

1 **Central vestibular tuning arises from patterned convergence of otolith afferents**

2

3 Zhikai Liu¹, Yukiko Kimura³, Shin-ichi Higashijima³, David G. Hildebrand⁴, Joshua L.
4 Morgan², Timothy E. Holy¹, Martha W. Bagnall¹

5

6 ¹Washington University in St. Louis, Neuroscience, St. Louis, MO,

7 ²Washington University in St. Louis, Ophthalmology, St. Louis, MO,

8 ³National Institute for Basic Biology, Neurobiology, Okazaki, Japan,

9 ⁴Rockefeller University, New York, NY

10 * Corresponding author: bagnall@wustl.edu

11

12 **Abstract:**

13 As sensory information moves through the brain, higher-order areas exhibit more
14 complex tuning than lower areas. Though models predict this complexity is due to
15 convergent inputs from neurons with diverse response properties, in most vertebrate
16 systems convergence has only been inferred rather than tested directly. Here we
17 measure sensory computations in zebrafish vestibular neurons across multiple axes *in*
18 *vivo*. We establish that whole-cell physiological recordings reveal tuning of individual
19 vestibular afferent inputs and their postsynaptic targets. An independent approach,
20 serial section electron microscopy, supports the inferred connectivity. We find that
21 afferents with similar or differing preferred directions converge on central vestibular
22 neurons, conferring more simple or complex tuning, respectively. Our data also resolve
23 a long-standing contradiction between anatomical and physiological analyses by
24 revealing that sensory responses are produced by sparse but powerful inputs from
25 vestibular afferents. Together these results provide a direct, quantifiable demonstration
26 of feedforward input convergence *in vivo*.

27 **Key words:** neural computation; sensory encoding; feedforward excitation;
28 vestibulospinal neuron; electrical synapse; high-pass tuning; sensorimotor
29 transformation; body balance

30 **Introduction**

31 Neurons compute information from many different synaptic inputs. A central
32 challenge in understanding neuronal circuits is determining how the tuning and
33 connectivity of these inputs affect the resulting computations. For example, neurons in
34 visual cortex exhibit simple or complex orientation tuning, which is thought to derive
35 from the convergence of presynaptic inputs with distinct tuning properties (Hubel and
36 Wiesel, 1962, Alonso and Martinez, 1998). Computational models of such input-output
37 relationships have fundamentally shaped the way we think of information processing in
38 the brain (Felleman and Van Essen, 1991, LeCun et al., 2015). However, these models
39 generally require assumptions about many parameters that can only be measured with
40 incompatible approaches: the tuning of the presynaptic population, input connectivity,
41 and synaptic strengths, as well as the activity of the postsynaptic neuron itself. Direct
42 measurements of these parameters simultaneously are prohibitively difficult in most
43 systems, making it hard to define neuronal computations *in vivo*.

44 Vestibulospinal (VS) brainstem neurons receive direct vestibular sensory inputs
45 from peripheral vestibular afferents (Boyle et al., 1992) and project to the spinal cord
46 (Boyle and Johanson, 2003). Understanding the neuronal computations of VS neurons
47 would not only inform how vestibular sensory signals are processed in the brain, but
48 also provide a mechanistic view of sensorimotor transformation. VS neurons, like other
49 central vestibular neurons, produce diverse responses to head movement. During head
50 tilt or acceleration, some central vestibular neurons exhibit simple cosine-tuned
51 responses, similar to those of the afferents: the strongest activity is evoked by
52 movements in a preferred direction, with little or no response in the orthogonal direction.
53 In contrast, other central vestibular neurons exhibit more complex responses, including
54 bidirectional responses (Peterson, 1970) and spatiotemporally complex tuning (Angelaki
55 et al., 1993). A vectorial model predicts that convergence of several simple cosine-
56 tuned afferents can fully account for the response of either a simple or a complex
57 central vestibular neuron, depending on whether those afferents are similarly tuned or
58 differently tuned (Angelaki, 1992). However, as in other systems, this model has been
59 technically challenging to test experimentally.

60 We chose to address this question in the small brain of the larval zebrafish. The
61 VS circuit was previously identified in the larval zebrafish as the homolog of mammals
62 (Kimmel et al., 1982), which becomes functional as early as 3 days post fertilization
63 (dpf) (Mo et al., 2010). The accessibility of the larval zebrafish brain for intracellular
64 recording from identified VS neurons allows us to investigate how central vestibular
65 neurons compute sensory signals in vertebrates.

66 Here we establish a novel approach to record sensory evoked responses *in vivo*
67 from VS neurons in the larval zebrafish. We find that individual afferents evoke large
68 amplitude-invariant excitatory postsynaptic currents (EPSCs), allowing us to separate
69 distinct afferent inputs that converge onto a given VS neuron. This provides a
70 mechanism to simultaneously measure the sensory tuning and synaptic strength of
71 each converging afferent, as well as the response of the postsynaptic neuron. We show

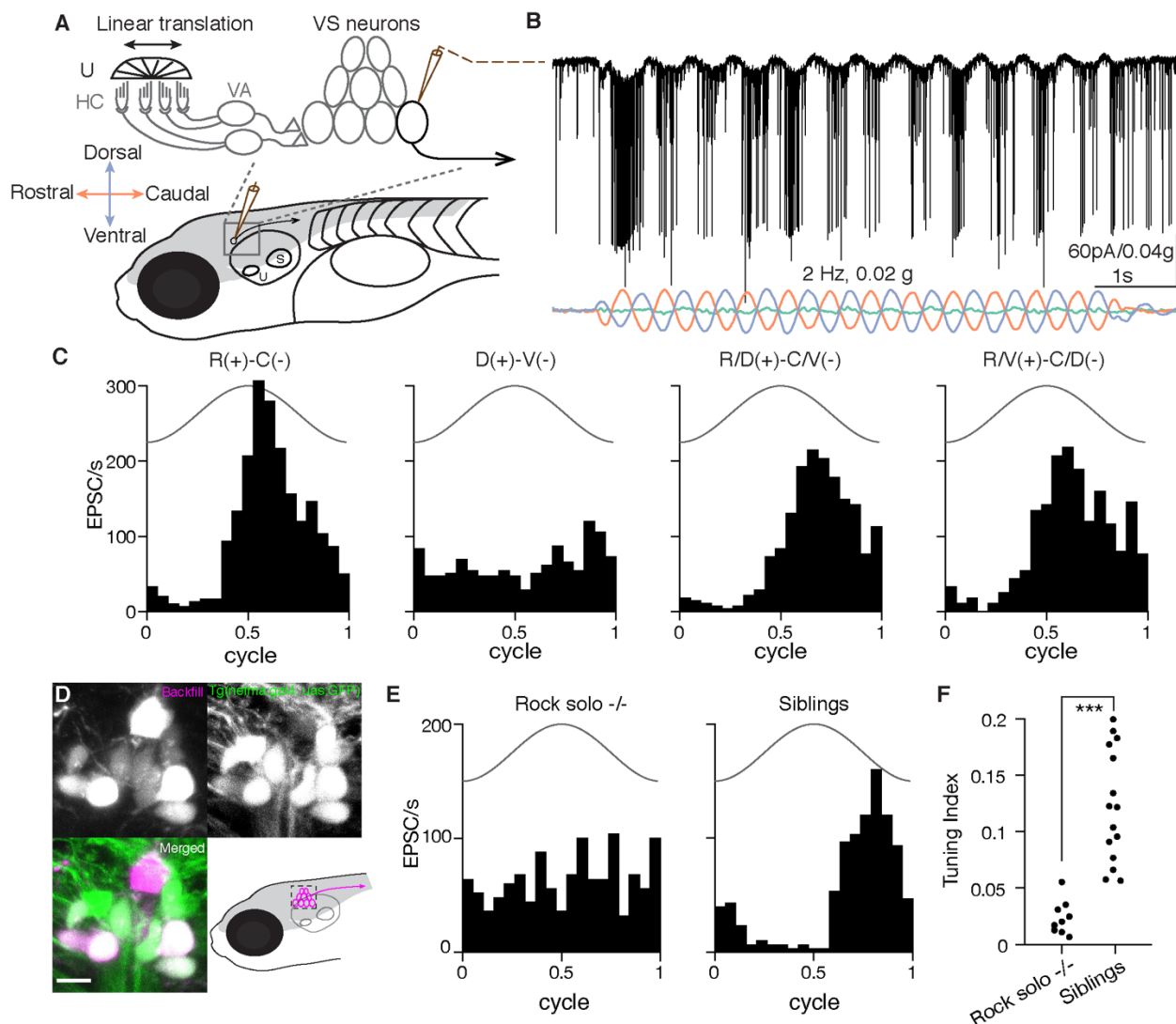


Figure 1: Sensory-evoked responses *in vivo* in vestibulospinal (VS) neurons

A. Schematic representing *in vivo* patch clamp recording configuration and vestibular afferent circuit in larval zebrafish, U: utricle, HC: hair cells, VA: vestibular afferents, S: saccule.

B. Example recording trace from a VS neuron in voltage clamp mode during 2 Hz, 0.02 g translational movement on the R/V(+)-C/D(-) axis. EPSCs, black; acceleration in three body axes, colored (orange, rostral[+]-caudal[-]; green, dorsal[+]-ventral[-]; blue, ipsilateral[+]-contralateral[-]).

C. Sensory-evoked EPSC responses to translation in four different axes for the same VS neuron as in B, across 12 cycles. Solid line, acceleration (2 Hz, 0.02 g).

D. Tg(gefma:gal4; UAS:GFP) (green) colabels VS neurons identified by dye backfilling (magenta) from spinal cord. Scale bar: 5 μ m

E. Sensory responses of a VS neuron in the best direction in a rock solo -/- (left) and in a het/WT sibling (right).

F. Summary of tuning index in the best direction for all VS neurons recorded in rock solo -/- (9 neurons, 5 fish) and siblings (15 neurons, 10 fish). Mann-Whitney U test, $p=6.5e-5$

72 that afferents with similar tuning direction preferentially converge, producing simple
73 tuning in the VS neuron. Furthermore, the smaller number of cells with complex
74 bidirectional responses receive input from differently tuned afferents, with consequent
75 simple or complex spiking. We also show that these afferent inputs are sufficient to
76 predict the tuning of the VS neuron. Together, this work reveals how central neurons in
77 the brain compute sensory information from their presynaptic inputs.

78 **Results:**

79 **Sensory evoked responses of vestibulospinal neurons *in vivo***

80 Traditionally, measurements of neuronal responses to vestibular stimuli have been
81 accomplished by unit recordings (Angelaki and Dickman, 2000, Schor et al., 1984,
82 Fernandez and Goldberg, 1976a). Directly measuring vestibular-evoked synaptic
83 currents in central neurons *in vivo* has been technically challenging (Arenz et al., 2008,
84 Chabrol et al., 2015). We designed a custom whole-cell electrophysiology rig to deliver
85 translational motion stimuli to 4-7 dpf larval zebrafish via an air-bearing motorized sled
86 (Fig. 1A). This setup allows intracellular measurement of sensory-evoked responses
87 from vestibulospinal (VS) neurons on multiple axes *in vivo* for the first time, to the best
88 of our knowledge. To target identified VS neurons, we generated a Tg(nefma:gal4;
89 UAS:GFP) line, whose labelling overlaps dye backfilling (Figs. 1D, S1) from the spinal
90 cord, consistent with evidence of *Nefm* expression in mammalian vestibular neurons
91 (Kodama et al., 2020). We recorded spontaneous EPSCs in voltage clamp, at overall
92 rates varying from 1 to 365 EPSC/s. Delivery of translational movement evoked
93 corresponding modulations in EPSC frequency (Fig. 1B). The extent of modulation
94 varied depending on the direction of the stimulus delivered across four different axes
95 (Fig. 1C). In this example neuron, EPSC rate was modulated most strongly in the
96 rostral-caudal (R-C) axis and weakly in the dorsal-ventral (D-V) axis, with intermediate
97 strength responses for the diagonal directions (R/D-C/V and R/V-C/D).

98 Response to translational movement could derive from the vestibular or other sensory
99 inputs. In larval zebrafish, the anterior otolith (utricle) is the sole functional vestibular
100 sensor (Riley and Moorman, 2000). To examine whether utricular signaling is necessary
101 for the observed tuning, we measured the sensory response of VS neurons in the
102 *otog*^{c.1522+2T>A} -/- (rock solo) animals, which lack the utricle (Mo et al., 2010, Roberts et
103 al., 2017). Translational stimuli were ineffective at modulating EPSC rate in VS neurons
104 of rock solo homozygotes in contrast to wild-type/heterozygous siblings (representative
105 examples, Fig. 1E). Across all recordings, VS neurons of rock solo -/- animals exhibit
106 largely untuned EPSCs compared to siblings, as quantified by a tuning index (Fig. 1F).
107 Thus, this approach reveals sensory-evoked synaptic responses encoding directional
108 vestibular stimuli in identified VS neurons *in vivo*.

109 **Mixed electrical and chemical synapses mediate the transmission from otolith
110 afferents to VS neurons**

111 What properties define the vestibular afferent synapse onto VS neurons? In
112 rodents, vestibular afferent synapses onto vestibulo-ocular reflex neurons exhibit

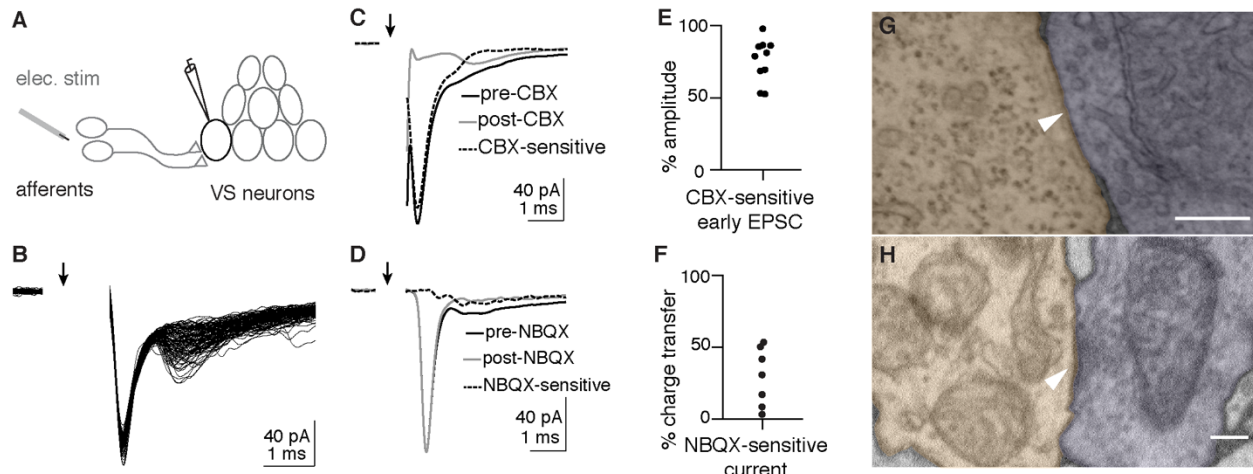


Figure 2: Otolith afferent to VS neuron transmission is mediated by mixed electrical and chemical synapses

- A. Schematic of whole-cell recording configuration from VS neuron while electrically stimulating otolith afferents.
- B. Example EPSCs evoked by electrical stimulation of the otolith afferents; 105 EPSCs overlaid. Arrow indicates onset of stimulation. Stimulus artifact is blanked.
- C. Carbenoxolone (CBX) diminishes the fast component of evoked EPSCs
- D. NBQX abolishes the second, slower component of evoked EPSCs
- E. Group data quantifying the reduction of early EPSC amplitude by CBX
- F. Group data quantifying the total charge transfer that is abolished by NBQX application
- G. Example EM image of gap junction between identified otolith afferent (pseudocolored purple) and VS neuron (orange). Scale bar: 200 nm.
- H. Example EM image of chemical synapse between otolith afferent (purple) and VS neuron (orange). Scale bar: 200 nm.

113 amplitude-invariant synaptic transmission, mediated by specialized vesicular release
114 machinery (Bagnall et al., 2008, McElvain et al., 2015, Turecek et al., 2017). To
115 characterize afferent synaptic input to VS neurons, we electrically stimulated the
116 vestibular (anterior statoacoustic) ganglion while recording from VS neurons in voltage
117 clamp (Fig. 2A). Stimulation evoked a synaptic current with two components. The first
118 component had fast kinetics with short latency (0.56 ± 0.28 ms, $n=8$), low jitter (0.05
119 ± 0.04 ms, $n=8$), and invariant EPSC amplitude (SD: $6.7 \pm 3.9\%$, normalized to peak)
120 across trials. In contrast, the second component had slower kinetics and variable
121 amplitudes (Fig. 2B). We dissected the two components of evoked EPSCs
122 pharmacologically. Bath application of the gap junction blocker carbenoxolone (CBX,
123 $500 \mu\text{M}$) during afferent stimulation substantially reduced the first component of the
124 EPSC (Figs. 2C, E). In contrast, bath application of the AMPA receptor antagonist
125 NBQX ($10 \mu\text{M}$) abolished the second component of synaptic current (Fig. 2D).
126 Furthermore, the fast EPSCs were not reversed by changing the holding potential (Fig.
127 S2), a signature behavior of electrical synaptic transmission (Akrouh and
128 Kerschensteiner, 2013). Thus, the early and late components of afferent-evoked
129 synaptic currents are mediated by gap junctions and AMPA receptors, respectively.
130 Across VS neurons, the NBQX-sensitive currents accounted for $27.1 \pm 20.2\%$ of total
131 charge transfer ($n=7$, Fig. 2F), demonstrating that gap junctional current is the major
132 component mediating synaptic transmission.

133 To evaluate ultrastructural evidence for mixed synaptic transmission, we re-
134 imaged existing serial ultrathin sections of a 5.5 dpf larval zebrafish (Hildebrand et al.,
135 2017) at sufficiently high resolution (1-4 nm/px) to identify synaptic contacts between
136 myelinated utricular afferents and VS neurons, identified anatomically. We found both
137 tight junction structures (Fig. 2G), and vesicles apposed to a postsynaptic density (Fig.
138 2H) at appositions between utricular afferent and VS neurons, consistent with
139 anatomical evidence for mixed electrical / chemical transmission at this synapse in adult
140 fish (Korn et al., 1977) and rat (Nagy et al., 2013). Together, these results demonstrate
141 that VS neurons receive vestibular afferent inputs mediated by amplitude-invariant gap
142 junctional (electrical) and variable amplitude glutamatergic (chemical) synapses.

143 **Inferring afferent tuning from distinct EPSCs**

144 Because electrically mediated EPSCs from afferents to VS neurons exhibited a
145 fixed amplitude, we hypothesized that we could distinguish the activity of individual
146 otolith afferents converging onto a given VS neuron by their characteristic EPSC
147 amplitudes. Indeed, spontaneous and sensory-evoked EPSCs recorded in VS neurons
148 often fell into distinctive size bins, as visualized in a histogram of EPSC amplitudes
149 (Figs. 3A, B). EPSCs were sorted into three clusters with unsupervised learning (see
150 Methods), primarily leveraging their amplitudes. Each of these EPSC clusters showed a
151 stereotypical amplitude and waveform in this example neuron (Fig. 3A, inset). To test
152 whether each cluster of EPSCs amplitudes corresponds to an individual afferent, we
153 used an approach derived from spike sorting: temporal autocorrelation to test for
154 refractory periods within EPSC event times. Physiologically, one afferent cannot
155 generate two action potentials within its refractory period (Fernandez et al., 1972); thus

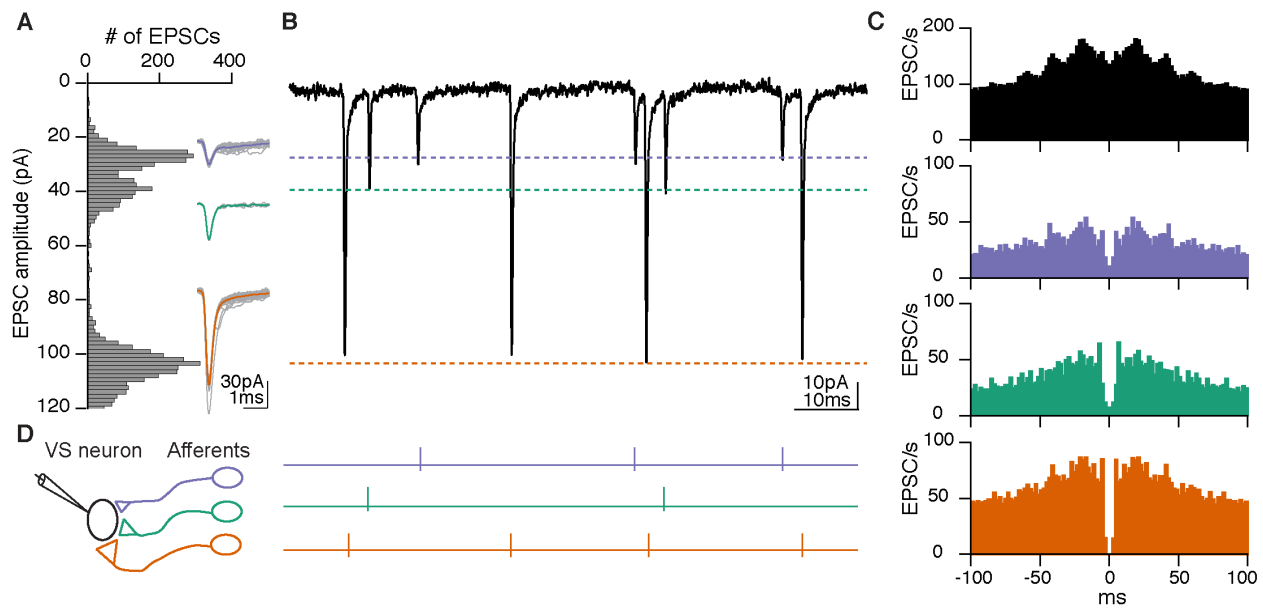


Figure 3: Distinct EPSC amplitudes reflect individual afferent inputs

A. Histogram of spontaneous and sensory-evoked EPSC amplitude distribution of the same VS neuron as Fig. 1B. Inset, overlay of individual EPSCs (gray) and average (colored) for each amplitude bin.

B. Example trace of EPSCs exhibiting stereotypic shapes and amplitudes in three clusters, corresponding to each amplitude bin in A.

C. Auto-correlogram of all EPSCs recorded from the VS neuron (top, black) or divided into three clusters based on EPSC amplitudes (bottom, colored). A refractory period around 0 ms only occurs for EPSCs within each cluster, but not across all EPSCs.

D. Schematic of three different otolith afferents converging onto one VS neuron, each eliciting EPSCs with a distinct amplitude (represented by different synaptic sizes). Right, spike activities of three afferents inferred from B.

156 the EPSCs elicited by that afferent should exhibit a refractory period as well. An auto-
157 correlogram of all EPSC event times in this example neuron did not display a refractory
158 period (Fig. 3C, top). In contrast, an auto-correlogram within each EPSC cluster
159 exhibited a clear refractory period around 0 ms (Fig. 3C, bottom). Furthermore, cross-
160 correlograms between EPSC clusters did not show this structure, consistent with the
161 notion that they arise from independent inputs (Fig. S3). Accordingly, we can interpret
162 these three EPSC clusters as deriving from the activity of three distinct presynaptic
163 afferents (Fig. 3D, left). Because of the high fidelity of electrical transmission, each
164 EPSC cluster effectively reads out the spiking of an individual afferent, allowing us to
165 measure presynaptic activity via postsynaptic recording (Fig. 3D, right).

166 To test this interpretation of electrophysiological data with a completely
167 independent approach, we reconstructed the whole volume of myelinated utricular
168 inputs onto 11 VS neurons from a high resolution re-imaged serial section EM dataset
169 acquired from the right side of one 5.5 dpf larval zebrafish (Fig. 4A, B). We found that
170 the connection between myelinated utricular afferents and VS neurons was relatively
171 sparse. All VS neurons were contacted by at least two utricular afferents, but some
172 afferents did not innervate any VS neurons (Fig. 4C). These reconstructions showed
173 that a range of 2-6 afferents (mean \pm std: 3.4 ± 1.4) converged onto each VS neuron (Fig.
174 4D). We compared these numbers to those derived from whole-cell physiology, where
175 we inferred the number of convergent afferents from the number of EPSC clusters.
176 Across all VS neuron recordings, we found a range of 0-5 afferents (1.7 ± 1.3) converged
177 onto each VS neuron (Fig. 4E). The result from anatomical reconstruction is largely
178 consistent with the overall distribution of afferent contacts as measured by whole-cell
179 physiology, presumably with some small-amplitude EPSCs elicited by the afferents not
180 successfully clustered. Therefore, these results demonstrate that synaptic inputs from
181 individual vestibular afferents can be separated by their stereotypic EPSC waveforms,
182 yielding inferred afferent convergence consistent with high-resolution anatomical
183 connectivity.

184 **Spatial tuning of inferred otolith afferents**

185 By recording from one VS neuron, we can infer the activity of its presynaptic
186 afferents. This approach thus offers a unique opportunity to measure the sensory tuning
187 of several convergent afferents simultaneously. To determine the spatial tuning of
188 convergent afferent inputs, we delivered 2 Hz, ±0.02 g sinusoidal translational stimuli
189 on four axes in the horizontal plane and recorded the sensory-evoked EPSCs, as
190 shown for an example VS neuron (Fig. 5A). In this example neuron, the inferred
191 utricular afferent (EPSC cluster) with the largest synaptic amplitude responded best to
192 caudally-directed acceleration, while two others responded with varying sensitivities to
193 rostrally-directed acceleration, in all cases with phase leads relative to peak
194 acceleration (Fig. 5B). With these measurements, we can derive the preferred tuning
195 direction, gain and phase of each afferent, as represented by the direction and length of
196 a vector (Fig. 5B, right). To validate the consistency of the vectorial representation, we
197 used a previously established approach (Schor et al., 1984) to quantify the tuning
198 vectors with separately measured responses to two circular stimuli (Fig. S4 B), which

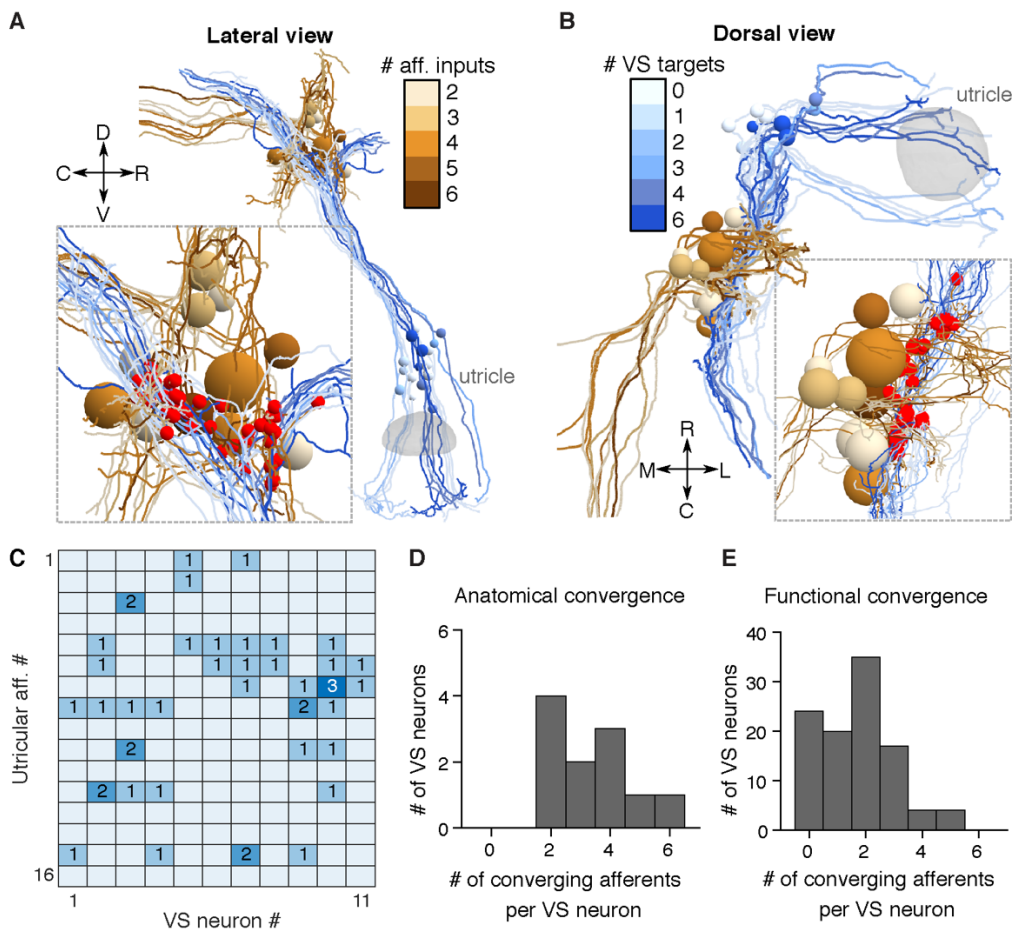


Figure 4: Anatomical reconstruction reveal similar convergence pattern as physiology

A. Serial-section EM reconstruction (lateral view) of all myelinated utricular afferents (blues) and VS neurons (browns) on the right side of one animal (5.5 dpf). Inset, identified synaptic contacts between afferents and VS neurons (red). Color scale represents number of distinct afferents synapsing with a given VS neuron (browns). VS neurons with greater number of afferent inputs are located more ventrally.

B. Dorsal view of the same reconstruction as A. Color scale represents number of VS neurons contacted by a given afferent (blues).

C. Number of distinct synaptic contacts from each utricular afferent onto each VS neuron, based on serial-section EM reconstruction.

D. Histogram of the numbers of distinct afferents converging onto each VS neuron, as measured by serial-section EM reconstruction (11 neurons, 1 fish)

E. Histogram of the numbers of distinct afferents converging onto each VS neuron, as inferred from whole-cell physiology recording (104 neurons, 89 fish)

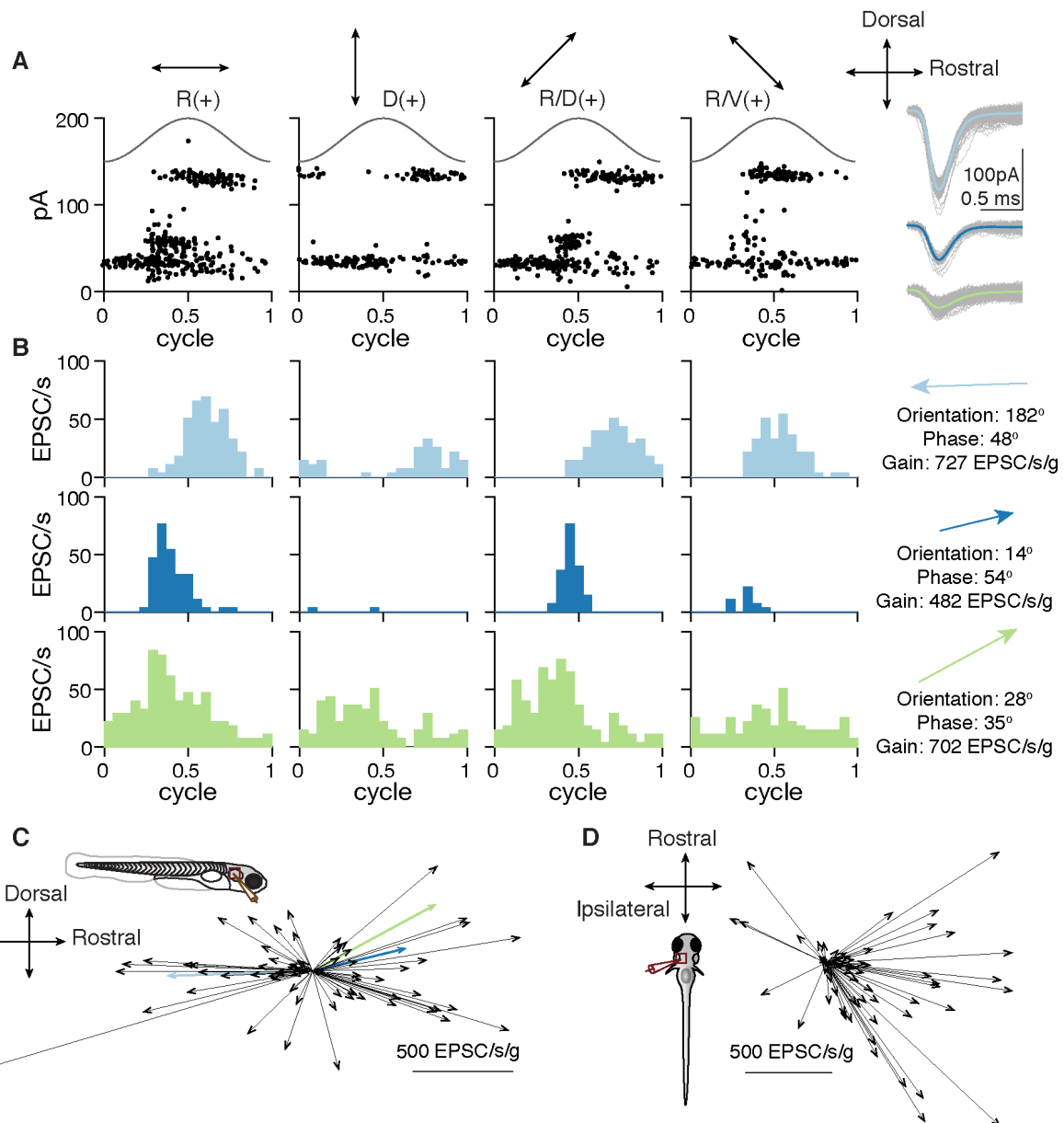


Figure 5: Spatial tuning of inferred otolith afferents

A. EPSC responses of an example neuron in response to 2 Hz, 0.02 g translational stimuli (solid sinusoidal line, acceleration) on 4 different axes (top, arrows). Each dot represents one EPSC; note three EPSC clusters with distinct amplitudes. Right, overlay of individual EPSCs (gray) and average (colored) for each cluster.

B. EPSC tuning of three clusters. Right, vectors representing the maximum tuning direction, phase, and gain of each inferred afferent corresponding to an EPSC cluster.

C. Maximum tuning directions of all afferents from VS neurons recorded from fish oriented side-up. Colored arrows represent tuning of afferents in B (69 afferents, 43 neurons, 33 fish)

D. Maximum tuning directions of all inferred afferents from VS neurons recorded from fish oriented dorsal-up. (60 afferents, 36 neurons, 36 fish)

199 showed similar preferred directions as those measured by translational stimuli (Figs. S4
200 A-C). Across all recordings with the animal oriented side-up, tuning of afferents was
201 strong in the rostral (30/69) and caudal (31/69) directions, but relatively weak in the
202 dorsal (4/69) and ventral (4/69) directions, as represented by an overlay of all inferred
203 afferent tuning vectors (Fig. 5C). When fish were oriented dorsal-up, the axes tested
204 were rostral-caudal and ipsilateral-contralateral (motion along an axis from one ear to
205 the other). In this position, most afferents were strongly tuned to acceleration towards
206 the contralateral direction (31/60), some exhibited preferential tuning to the acceleration
207 to the rostral (4/60) and caudal (20/60) directions, and only 5/60 afferents were tuned to
208 the ipsilateral direction (Fig. 5D). These results showed that each afferent in the larval
209 zebrafish exhibits selective responses to different translational stimuli. Afferents overall
210 responded best to acceleration towards the contralateral, rostral and caudal directions,
211 which correspond to ipsilateral, nose-up and nose-down tilts in postural change
212 (Angelaki and Cullen, 2008), consistent with the distribution of hair cell polarity in the
213 utricular macula (Haddon et al., 1999).

214 **Temporal tuning of inferred otolith afferents**

215 The sensitivity and phase of vestibular afferents varies for motion at different
216 frequencies (Fernandez and Goldberg, 1976b). The tuning of otolith afferents ranges
217 from typically more jerk-encoding (derivative of acceleration) at low frequencies to more
218 acceleration-encoding at high frequencies. What temporal tuning profile do afferents in
219 larval zebrafish exhibit? We applied translational stimuli with different frequencies (0.5-8
220 Hz, ± 0.02 g) on the rostral-caudal axis. In the example neuron, all three inferred otolith
221 afferents showed similar tuning, with progressively stronger responses with increasing
222 frequencies of stimulation (Fig. 6A). Across group data acquired at both ± 0.02 g and
223 ± 0.06 g, the average tuning gain increased 3.3-fold (0.02 g) and 2.3-fold (0.06 g) from
224 0.5 Hz to 8 Hz (Fig. 6B). Most afferents (39/48) showed at least 2-fold increase from 0.5
225 Hz to 4 Hz in tuning gain at either 0.02 g or 0.06 g. Only one afferent had relatively flat
226 gain (< 50% increase) at both 0.02 g and 0.06 g, and its tuning was overall weak (mean
227 gain: 1.88 and 2.24 EPSC/s respectively), suggesting it was less sensitive or not tuned
228 on the rostral-caudal axis. Regardless of tuning direction (rostral: 44%, 21/48; caudal:
229 56%, 27/48), afferents exhibited a phase lead relative to peak acceleration at various
230 tested stimulus magnitudes and frequencies ((Fig. 6C, S5). On average, the phase lead
231 at low frequency (0.5 Hz) was 84.0° for 0.02 g and 78.6° for 0.06 g. At high frequency (8
232 Hz), the phase lead was reduced to 33.6° for 0.02 g and 39.3° for 0.06 g. The temporal
233 dynamics of the afferents resembled those of previously reported irregular units
234 (Goldberg et al., 1990), with low spontaneous firing rates (10.28 \pm 9.1 EPSC/s) and
235 larger coefficients of variation (CV). The average CV across inferred afferents was
236 0.97 \pm 0.24, and the smallest CV was 0.5 (Fig. S6), indicating that no regular-firing otolith
237 afferents were detected synapsing onto VS neurons. We conclude that the otolith
238 afferents act as a high-pass filter, encoding a mixture of acceleration and jerk, similar to
239 otolith afferents in primates (Laurens et al., 2017).

240 **Preferential convergence**

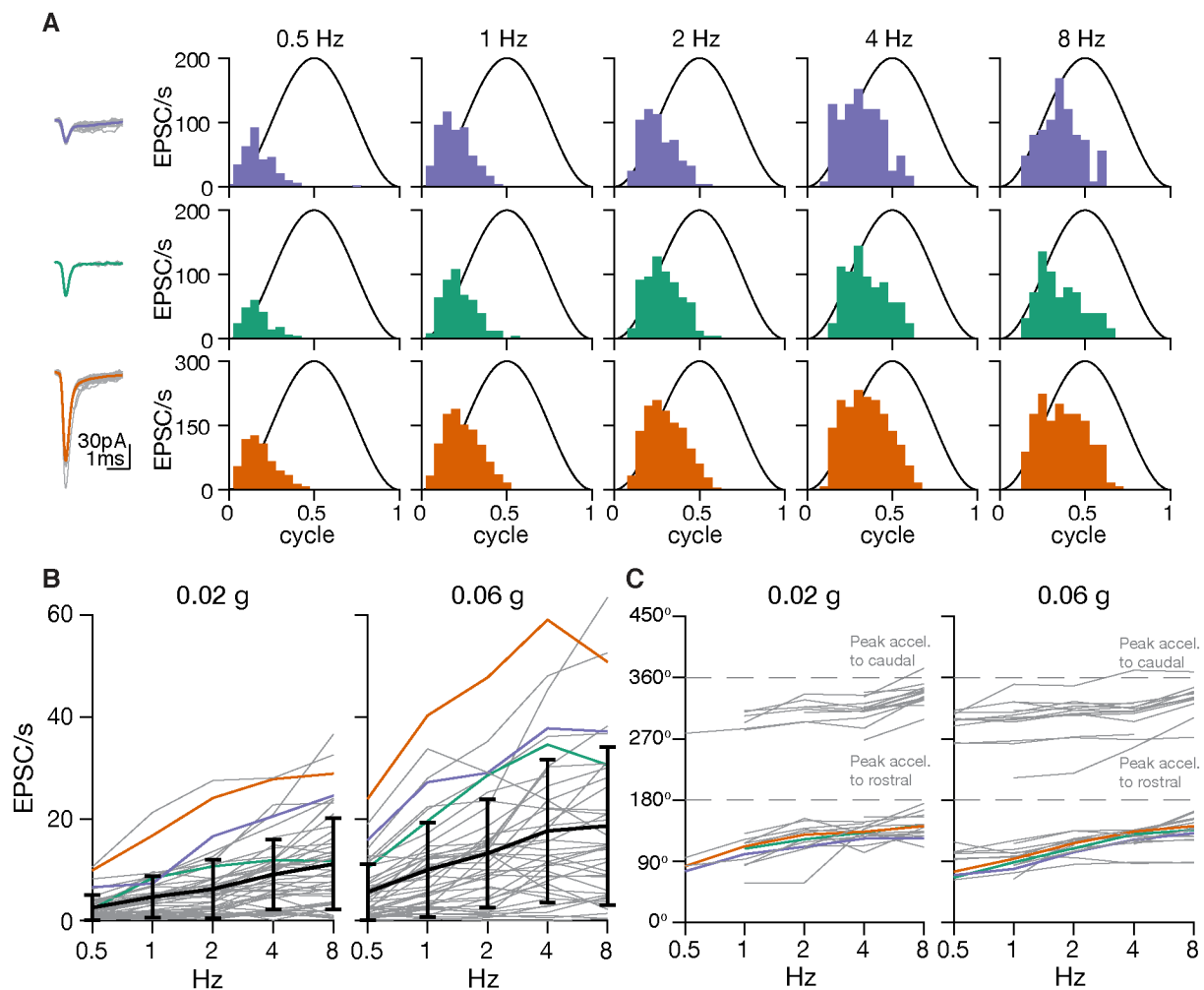


Figure 6: Temporal tuning of inferred otolith afferents

A. Sensory tuning of afferent inputs to one VS neuron during translational movement at 5 different frequencies in the rostral(+)–caudal(–) axis. Left, EPSC waveforms of three different clusters recorded from one VS neuron. Right, temporal tuning profile of each EPSC cluster on the rostral-caudal axis.

B. Gains of inferred afferents across different frequencies of translational acceleration. Gray, individual afferents; colored, afferents from A; black, mean and standard deviation of gains from all afferents (0.02 g, 48 afferents; 0.06 g: 46 afferents; 25 neurons, 20 fish)

C. Phases of inferred afferents across frequencies, relative to sinusoidal stimulus. 180° (0.5 cycle in A) represents the peak of acceleration towards rostral direction; 360° represents the peak of acceleration towards caudal direction (0 or 1 cycle in A). Data were thresholded to only include afferents whose gain was > 5 EPSC/s (0.02 g, 36 afferents; 0.06 g, 38 afferents; 25 neurons, 20 fish)

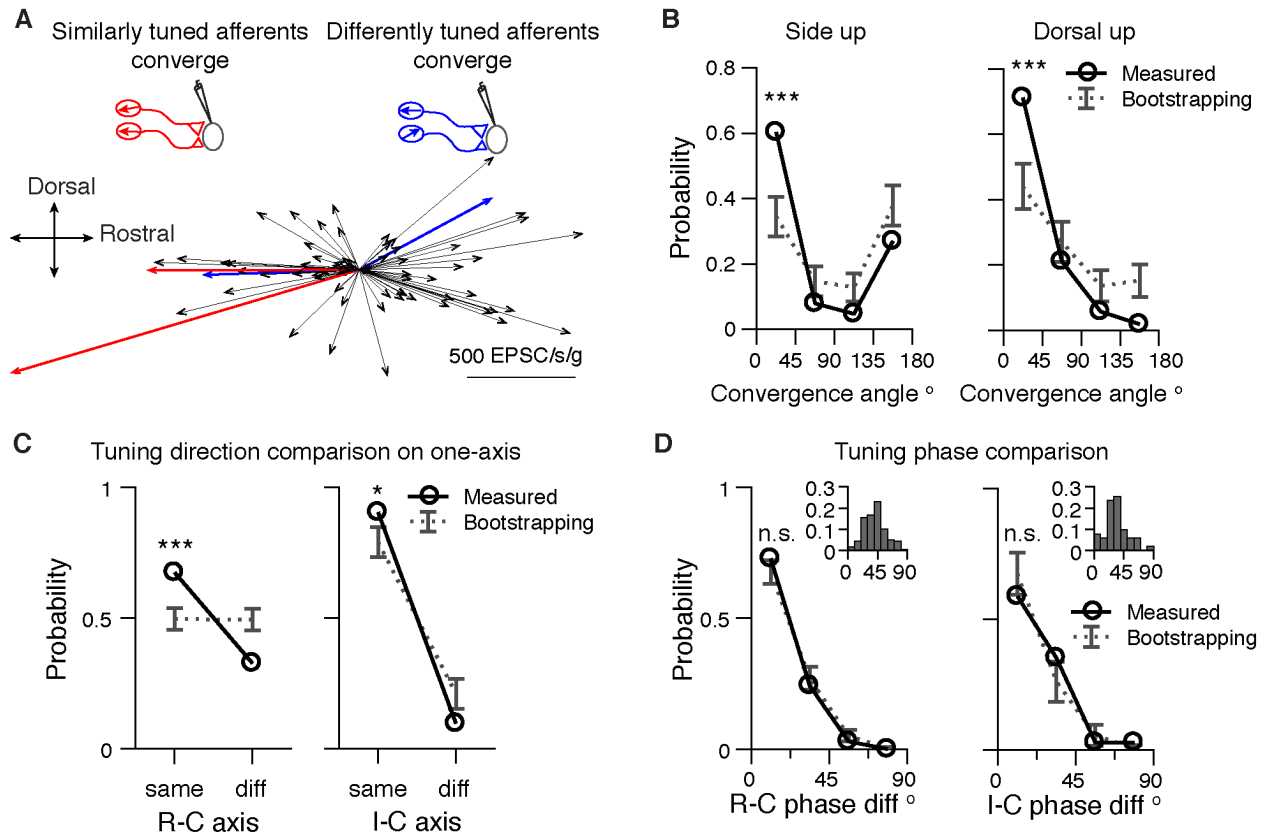


Figure 7: Afferents with similar tuning direction preferentially converge

A. Example of two pairs of converging afferents from two VS neurons in side-up fish. Red, converging afferents are similarly tuned, with small convergent angle between the pair; Blue: converging afferents are differently tuned, with large convergent angle between the pair.

B. Probability distribution of converging angles for measured and randomly generated afferents pairs in side up fish and dorsal up fish. Two tailed z-test, side up, 0-45°: $p=2e-5$, 135-180°: $p=0.08$. (63 afferent pairs); dorsal up, 0-45°: $p=8e-5$, 135-180°: $p=0.007$. (52 afferent pairs)

C. Probability distribution of converging afferents tuned to the same direction vs different direction, on the rostral-caudal and ipsilateral-contralateral axis. Two tailed z-test, R-C, same: $p=1e-5$, diff: $p=4e-5$ (150 afferent pairs); I-C, same: $p=0.044$, diff: $p=0.044$ (52 afferent pairs).

D. Probability distribution of phase difference for converging afferents, on the rostral-caudal and ipsilateral-contralateral axis. Two tailed z-test, R-C, 0-22.5° $p=0.26$ (103 afferent pairs); I-C, 0-22.5°, $p=0.28$ (34 afferent pairs). Inset: distribution of tuning phase of afferents, R-C, 177 afferents; I-C, 60 afferents; 90° represents the peak of acceleration of preferred direction (2 Hz, 0.02 g).

241 Individual VS neurons can receive inputs from afferents with similar (Fig. 6A) or
242 different tuning (Fig. 5B). Is afferent tuning convergence random or structured? The
243 responses of inferred afferents that converge onto the same VS neuron were
244 represented by their tuning vectors (Fig. 7A). The angle between the vectors indicates
245 the similarity of convergent inputs, with a small angle for a VS neuron with similarly
246 tuned inputs and a large angle for a VS neuron with differently tuned inputs. From 43
247 VS neurons recorded in the side-up orientation, 60% (38/63) of converging afferent
248 pairs had small angles ($<45^\circ$) and 27% (17/63) had large angles ($>135^\circ$). Compared to
249 a random pairing angle distribution generated by bootstrapping, the percentage of
250 similarly tuned convergent afferent pairs was significantly higher than chance (Fig. 7B,
251 left). From 36 VS neurons recorded in the dorsal-up orientation, there were 71% (37/52)
252 of inferred afferent pairs with a converging angle smaller than 45° , and only 2% (1/52)
253 with a converging angle larger than 135° due to the small number of ipsilaterally tuned
254 afferents (Fig. 5D). Nonetheless, the probability of similarly tuned afferent convergence
255 ($<45^\circ$) was significantly higher than that chance (Fig. 7B, right). For afferent pairs with
256 converging angle larger than 45° (45° - 90° , 90° - 135° , 135° - 180°), their probabilities was
257 slightly lower than their respective estimated distribution by bootstrapping. Accordingly,
258 on a given body axis (R-C or I-C), convergent afferents are also more likely to encode
259 similar tuning directions (Fig. 7C). These results suggest that afferents with similar
260 tuning direction preferentially converge at rates exceeding what would be expected by
261 random connectivity.

262 Do converging afferents also have similar tuning phase regardless of their tuning
263 direction? Most afferents are phase-leading with 2 Hz, 0.02 g stimulation (Figs. 6 and
264 7D, inset), and the phase difference between afferents is small (R-C: $41^\circ \pm 16^\circ$, n=177,
265 I-C: $33^\circ \pm 17^\circ$, n=60). Consequently, most afferent pairs (R-C, $68 \pm 4.6\%$; I-C, $68 \pm 8\%$)
266 selected randomly have very small phase difference (phase diff. $< 22.5^\circ$) (Fig. 7D). Both
267 the probability of converging afferents having similar phase (phase diff. $< 22.5^\circ$) (R-C,
268 73%, 75/103; I-C, 59%, 20/34) and the cumulative distribution (Fig. S7) lay within the
269 bootstrap predictions on the rostral-caudal and ipsilateral-contralateral axes.
270 Therefore, tuning phase between converging afferent pairs is similar, in accordance with
271 their relatively homogeneous distribution.

272 In conclusion, we found that afferents forming synaptic connections with the
273 same postsynaptic VS partner typically have similar spatiotemporal tuning properties. In
274 particular, afferents with similar tuning direction preferentially converge, which explains
275 the long-standing observation that most VS neurons exhibit simple cosine tuning
276 (Peterson, 1970, Schor et al., 1984). However, a non-negligible number of VS neurons
277 receive convergent input from differently tuned afferents, a potential source for the
278 complex spatiotemporal tuning of central vestibular neurons.

279 **Complexity of central tuning is determined by the similarity of afferent inputs.**

280 Complex sensory tuning of central neurons is thought to arise from convergence
281 of more simply tuned inputs with differing spatial and temporal properties, in vestibular
282 (Angelaki et al., 1993), as well as visual (Jia et al., 2010) and somatosensory (Petersen,
283 2007, Roy et al., 2011) systems. For example, complex tuning such as bidirectional

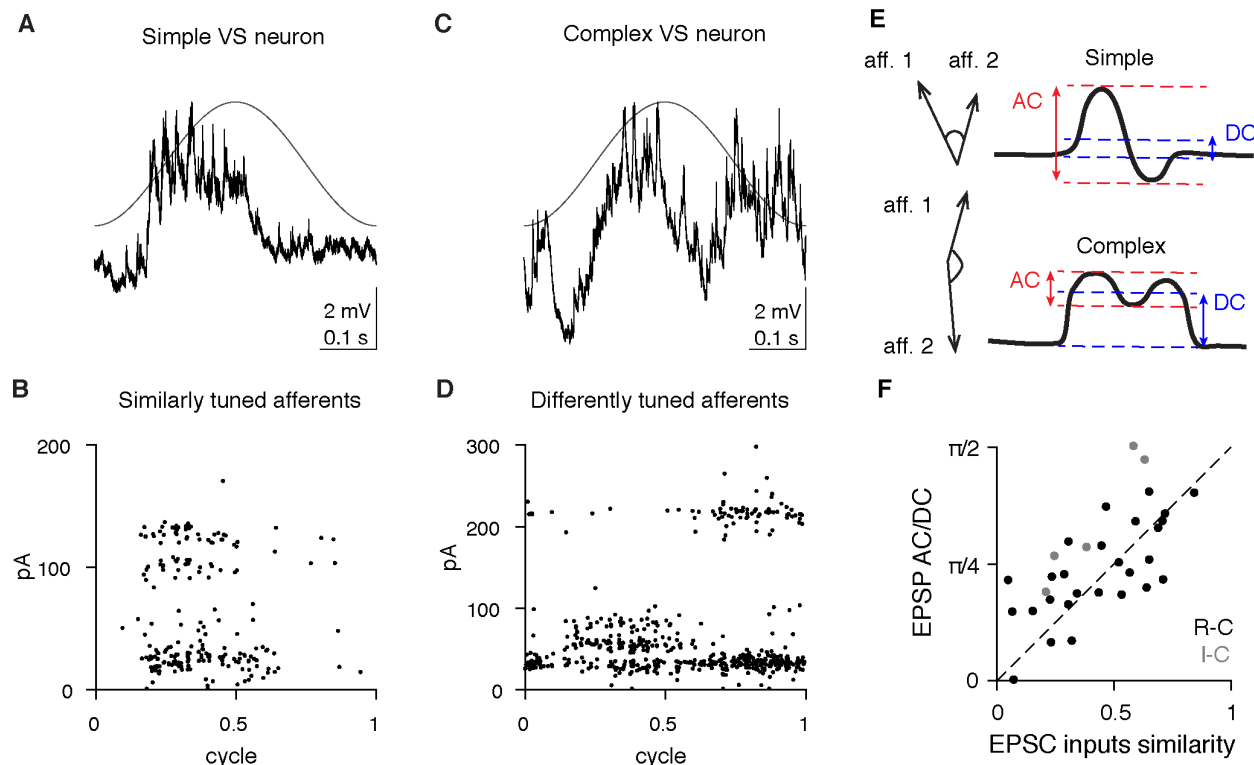


Figure 8: Subthreshold tuning responses of VS neurons are explained by the similarity of tuning of afferent inputs

A. Average membrane potential change in a VS neuron with simple response to 2 Hz, 0.02 g translational movement on the rostral(+)–caudal(–) axis.

B. EPSC responses for the simple cell shown in A. All inferred afferents exhibit similar tuning.

C. Average membrane potential change in a VS neuron with complex subthreshold response to 2 Hz, 0.02 g translational movement on the rostral(+)–caudal(–) axis

D. EPSC responses for the complex cell shown in B. Different inferred afferents exhibit distinct tuning, as shown by the different temporal responses of the large amplitude and medium amplitude EPSCs.

E. Schematic of different magnitudes of AC and DC responses in a simple and complex cell. Left, the hypothesized models of similarly tuned or differently tuned convergent afferent inputs underlying simple or complex responses, respectively.

F. Correlation of EPSC inputs similarity index and EPSP AC/DC response ratio (see Methods), for all non-spiking VS neurons with multiple convergent afferents. Sensory tuning of afferent inputs and EPSPs was measured on the R-C axis (black, $n=27$) and I-C axis (grey, $n=5$). Dashed, unity line. Pearson's R: 0.67

284 (Peterson, 1970) and broadly tuned sensory responses (Angelaki, 1992) of central
285 vestibular neurons can be computationally reconstructed from multiple modelled cosine-
286 tuned inputs. However, directly measuring these inputs has been technically difficult,
287 and it is unclear whether such models can sufficiently explain the activity of central
288 neurons. Therefore, we took advantage of the inferred afferent spiking to examine
289 whether the tuning of VS neurons can be constructed from the convergence of otolith
290 afferents.

291 We observed that different VS neurons showed simple or complex membrane
292 potential responses to translational stimuli on the rostral-caudal axis. An example
293 simple cell was only depolarized during a specific phase of acceleration (Fig. 8A),
294 whereas a complex cell exhibited multiple depolarized periods during the stimulus (Fig.
295 8C). Next, we measured the EPSC tuning in the same VS neurons. In the example
296 simple neuron, sensory evoked EPSCs exhibit three distinct amplitudes (Fig. 8B),
297 indicating three afferents converge onto the cell. These three afferents showed similar
298 tuning to each other, with strongest responses for rostrally-directed acceleration. In
299 contrast, the four inferred afferents that converge onto the example complex cell
300 exhibited a different tuning pattern. Two afferents were tuned to rostrally-directed
301 acceleration and the other two to caudally-directed acceleration (Fig. 8D).

302 To examine this relationship across the population, we defined an afferent inputs
303 similarity index for multiply innervated VS neurons, based on the phase of afferent
304 inputs and their EPSC amplitudes. The index ranges from 0-1, with smaller index
305 representing more divergent EPSC input tuning and larger index representing more
306 similar tuning (see Methods). A classifier originally developed for visual cortical neurons
307 was used to quantify the tuning complexity of the postsynaptic neuron's membrane
308 potential responses to sensory stimuli (Skottun et al., 1991). In this metric, neurons with
309 simple tuning show large AC and small DC responses, whereas complex cells exhibit
310 small AC and large DC responses (Fig. 8E). We found that the AC/DC ratio of the
311 membrane potential was strongly correlated with the similarity index of afferent inputs
312 (Fig. 8F). In other words, convergence of more similarly tuned afferents yields a more
313 simple VS neuron response, and the convergence of more differently tuned afferents
314 generates a more complex postsynaptic response.

315 **Spike tuning generation from similar and differently tuned afferents.**

316 We next extended the comparison of presynaptic to postsynaptic tuning by
317 measuring the spiking responses of VS neurons during sensory stimulation. In a subset
318 of VS neurons, the largest translational stimuli that we could deliver while holding the
319 cell was sufficient to evoke postsynaptic firing; in other neurons, a small bias current
320 was injected to evoke spiking during sensory stimulation (see Methods). Most VS
321 neurons exhibited simple spike tuning, and received convergent inputs from similarly
322 tuned afferents (Fig. 9A). Some VS neurons with simple spike responses received
323 convergent inputs from differently tuned afferents (Fig. 9B). Finally, complex spike
324 tuning in VS neurons was always generated by inputs from differently tuned afferents
325 (Fig. 9C). These three categories of input-output transformation (similar to simple,
326 different to simple, different to complex) were identified across all recordings from VS

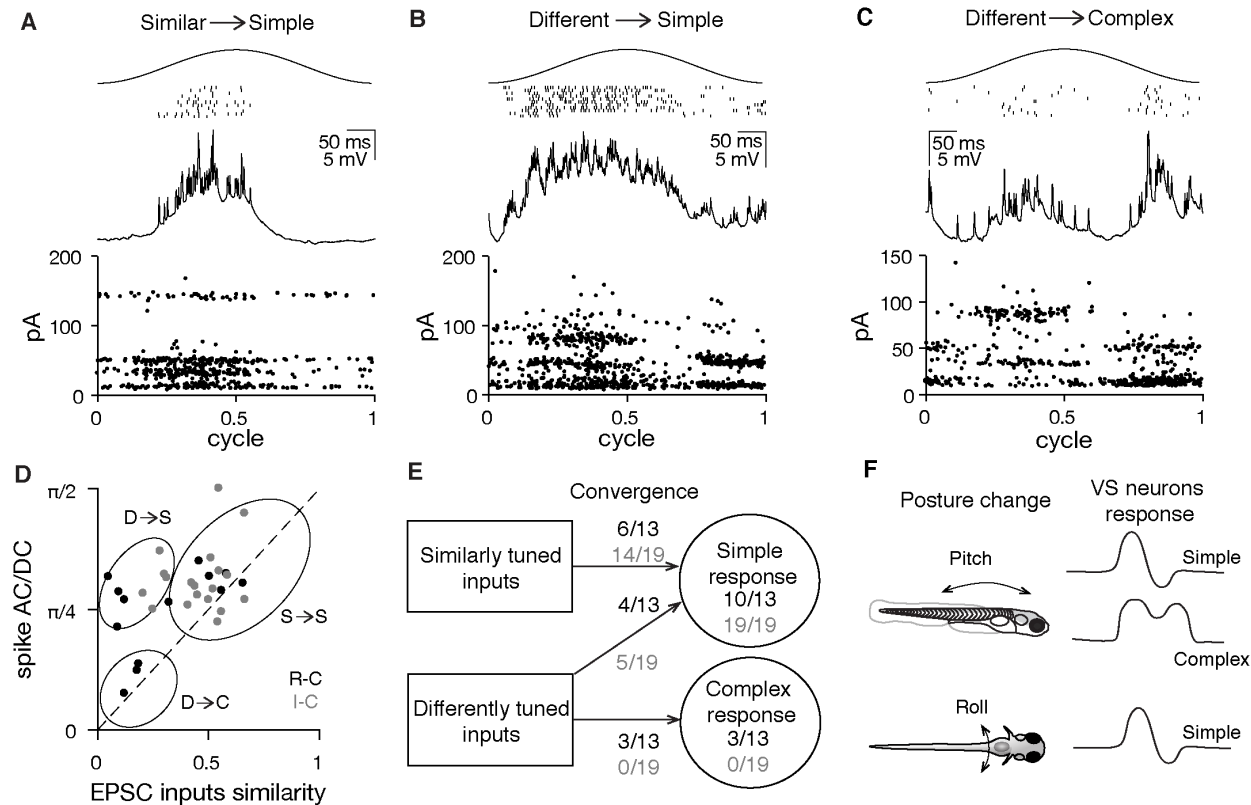


Figure 9: Spiking tuning complexity of VS neuron is partially explained by the similarity of tuning for the afferent inputs

- A. Example cell showing that simple spiking tuning response is constructed from afferent inputs with similar tuning direction. Top, sensory-evoked spike raster of a VS neuron during 2 Hz, 0.02 g translational movement on the I(-)-C(+) axis (11 trials); middle, average membrane potential of the VS neuron (11 trials); bottom, sensory-evoked EPSC response (12 trials); each dot represents one EPSC.
- B. As in A, for an example cell showing simple spiking tuning response arising from afferent inputs with different tuning directions on the I(-)-C(+) axis.
- C. As in A, for an example cell with a complex spiking tuning response due to afferent inputs with different tuning directions on the R(+)-C(-) axis.
- D. Correlation of EPSC input similarity index and spike activity AC/DC ratio, for all spiking VS neurons on the R-C axis (black, n=13 recordings) and I-C axis (gray, n=19). Circles, three categories of input-output transformation, corresponding to examples in A, B and C. Dashed, unity line. Pearson's R: 0.51
- E. Quantification of input-output transformation of VS neurons; Ns represent individual cells.
- F. Summary of different responses of VS neurons responding to posture change on the pitch and roll axes.

327 neurons (Fig. 9D). In total, most recordings (R-C, 6/13; I-C, 14/19) exhibited simple
328 spike tuning, of which 69% (20/29) received inputs from similarly tuned afferents, and
329 31% (9/29) received inputs from differently tuned afferents (Fig. 9E). Thus, convergence
330 of similarly tuned afferents yields simple spike tuning, but convergence of differently
331 tuned afferents can yield either simple or complex spike tuning. Interestingly, complex
332 spike tuning was only observed on the R-C axis (3/13 recordings), which subserves
333 pitch movements, not the I-C axis (0/19), which subserves roll (Fig. 9F). These results
334 indicate that VS neurons may play different roles in maintaining body balance on
335 different body axes.

336 **Discussion**

337 **Sensory convergence in the central vestibular nuclei**

338 Taking advantage of the invariant synaptic transmission of electrical synapses,
339 we separated distinct afferent inputs that converge onto VS neurons and measured the
340 spatial and temporal tuning of each converging afferent *in vivo*. This analysis is
341 facilitated by the sparseness of connectivity, with < 6 afferents synapsing with each VS
342 neuron. These data resolve a conflict in the literature: anatomically, very few otolith
343 afferent terminals are observed in the lateral vestibular nucleus (Newlands and
344 Perachio, 2003), but physiologically, afferent stimulation elicits monosynaptic EPSPs in
345 VS neurons (Boyle et al., 1992). Our data reveal that sparse but powerful afferent
346 synaptic contacts, located on the lateral dendrites of VS neurons, are sufficient to drive
347 the membrane potential of the cell during sensory stimulation. Although these large
348 afferent inputs drive sensory responses, VS neurons receive a wealth of non-vestibular
349 synaptic contacts on their large dendritic arbors. This is consistent with previous
350 findings that the activity of VS neurons is regulated by locomotion (Orlovsky, 1972),
351 proprioception (Neuhuber and Zenker, 1989), and other inputs (Sarkisian, 2000, Witts
352 and Murray, 2019). Interestingly, lateral geniculate neurons (LGN) of the visual
353 thalamus display a similar pattern of connectivity, with sparse, powerful afferent inputs
354 from retinal ganglion cells and weaker, diverse inputs from other sources (Usrey et al.,
355 1999, Sherman, 2005). Our findings suggest that this configuration is common to VS
356 neurons as well.

357 Similarly tuned otolith afferents preferentially converge onto VS neurons (Fig. 7),
358 demonstrating that feedforward excitation can generate central neurons with simple
359 response properties. In a similar vein, thalamocortical inputs with similar angular tuning
360 also preferentially project onto the same site in somatosensory cortex, and the preferred
361 tuning direction of the cortical neuron can be predicted by that of the presynaptic
362 thalamic neuron (Bruno et al., 2003). Furthermore, we found that convergence of
363 differently tuned afferents can yield a more complex postsynaptic response in central
364 vestibular neurons, similar to bidirectional or complex tuning observed previously in cats
365 (Peterson, 1970) and primates (Angelaki and Dickman, 2000). This result generally
366 supports the hypothesized model (Angelaki, 1992) that the tuning of central vestibular
367 neurons can be constructed from cosine tuned inputs with varying tuning properties.
368 However, we find that convergence of differently tuned afferents can also yield simple
369 tuning in VS neurons (Fig. 8B), suggesting other factors such as inhibition (Straka and

370 Dieringer, 1996) and thresholding (Priebe et al., 2004) might be involved. We found no
371 evidence for polysynaptic excitatory circuits during afferent stimulation (Fig. S9 A and
372 B), and modelling indicates that excitatory synaptic input is sufficient to predict
373 subthreshold membrane potential and tuning (Fig. S9 C-F). However, stronger stimuli
374 might elicit inhibition and other nonlinearities. Across brain regions, sensory tuning of
375 central neurons is constructed by a variety of mechanisms. These include afferent
376 convergence pattern (Alonso and Martinez, 1998, Priebe and Ferster, 2012), local
377 excitatory or inhibitory modulation (Wilent and Contreras, 2005), and nonlinear dendritic
378 computation (Lavzin et al., 2012). Our results demonstrate that sensory response of a
379 central neuron can be constructed from the afferent inputs in a direct feedforward
380 manner.

381 **Otolith afferent tuning properties in the larval zebrafish**

382 The derived spatial tuning profile of afferents in the larval zebrafish is similar to
383 the polarity of the hair cells in otolith macula, consistent with results in fish (Fay, 1984,
384 Platt, 1977) and primates (Fernandez et al., 1972). Notably, tuning to dorsal or ventral
385 acceleration was relatively weak for most afferents, presumably due to the horizontal
386 orientation of the utricular membrane in larval zebrafish inner ear. Afferents were
387 preferentially tuned to contralateral acceleration (ipsilateral tilt) in the roll axis, consistent
388 with the dearth of ipsilaterally tuned hair cells in larval zebrafish (Haddon et al., 1999).
389 In species with more centrally located line of polarity reversal (Fernandez and Goldberg,
390 1976a, Tomko et al., 1981), we would predict more convergence of oppositely tuned
391 afferents, and correspondingly more complex response of VS neurons in the roll axis,
392 as seen in cats (Peterson, 1970).

393 A significant question in vestibular systems is whether central vestibular neurons
394 receive selective projections from afferents with regular as opposed to irregular firing.
395 Both regular and irregular afferents are thought to converge on VS and vestibulo-ocular
396 reflex neurons in mammals, based on studies comparing recruitment thresholds of
397 afferent inputs (Boyle et al., 1992). Our data provide direct evidence that vestibular
398 inputs to VS neurons exhibit classic characteristics of irregular afferents (Eatock and
399 Songer, 2011): high-pass tuning, low spontaneous firing rate, and high CV of firing (Fig.
400 S6). It is unknown whether regular utricular afferents exist in the larval zebrafish.
401 Although regular utricular afferents were observed in guitarfish (Budelli and Macadar,
402 1979), they appear absent in toadfish (Maruska and Mensinger, 2015) and sleeper goby
403 (Lu et al., 2004). Based on serial section EM, many afferents make no contacts with VS
404 neurons (Fig. 4C), leading us to conclude that either regular afferents have not yet
405 developed or that they do not contact VS neurons in the larval zebrafish.

406 **Linear and fast synaptic transmission via gap junctions**

407 Our data reveal that electrical synapses mediate linear synaptic transmission
408 from otolith afferents to the VS neurons. In contrast, synaptic transmission at
409 retinotectal afferents in larval zebrafish is mediated solely by glutamate (Smear et al.,
410 2007), suggesting that electrical synapses in vestibular afferents are perhaps not simply
411 a feature of early larval development but play an important role in circuit computations,

412 potentially via their amplitude invariant transmission. Interestingly, mammalian
413 vestibular afferent synapses also exhibit amplitude invariant transmission in the medial
414 vestibular nucleus (Bagnall et al., 2008) and cerebellum (Arenz et al., 2008, Chabrol et
415 al., 2015), but via specialized glutamatergic terminals (Turecek et al., 2017, McElvain et
416 al., 2015), indicating that frequency-independent transmission is a hallmark of vestibular
417 signaling across vertebrates. Furthermore, mixed electrical and chemical synapses
418 have been anatomically identified between vestibular afferents and VS neurons in both
419 adult fish (Korn et al., 1977) and rodents (Nagy et al., 2013), suggesting the mixed
420 synapse may be a conserved mechanism across species to implement fast, frequency-
421 independent transmission in the lateral vestibular nucleus. The amplitude invariance of
422 this connection allowed us to examine whether there was any relationship between an
423 afferent's sensory gain or firing rate and the synaptic amplitude it evokes in a VS
424 neuron. No correlation appeared in either of these measures (Fig. S8), indicating that at
425 least within this population, synapse size is not "normalized" by firing rate.

426 **VS pathway underlying sensorimotor transformation**

427 The VS pathway is important for posture control. Larval zebrafish swim at high
428 frequencies up to 100 Hz (McLean and Fethcho, 2009) and are naturally unstable in
429 water (Ehrlich and Schoppik, 2017). Our study examined the response of VS neurons
430 with translational stimuli in the range of 0.04-0.12 g and 0.5-8 Hz, head movement
431 parameters comparable to slow swimming (Voesenek et al., 2016) or small angle tilting
432 motion in the larval zebrafish. In the roll axis all VS neurons are tuned to ipsilateral tilt
433 (Fig. S10), consistent with data from calcium imaging (Migault et al., 2018, Favre-Bulle
434 et al., 2018), suggesting they might excite specific motor units in the spinal cord to
435 produce compensatory movements (Bagnall and McLean, 2014). On the pitch axis, VS
436 neurons have more heterogeneous responses, including simple tuning to either rostral
437 or caudal acceleration (Fig. S10), as well as complex responses (Fig. 9E) to both
438 directions. Thus, when the animal is destabilized by excessive nose-up or nose-down
439 tilts, VS neurons might activate non-specific motor units, increasing the likelihood of
440 swim bouts to regain balance (Ehrlich and Schoppik, 2017).

441 The high-pass tuning and phase lead of otolith afferents innervating VS neurons
442 will make larvae most sensitive to ongoing changes in tilt or acceleration, especially at
443 high frequency. These data are consistent with behavioral observations that larvae
444 become more likely to swim to correct their position in the pitch axis when angular
445 velocity (i.e., changing tilt) reaches a critical threshold (Ehrlich and Schoppik, 2017).
446 This compensatory postural adjustment, which relies on both trunk and fins, is absent in
447 *rock solo* larvae (Ehrlich and Schoppik, 2019), in line with our results on the absence of
448 sensory tuning in those animals. Larval VS neurons receive similar amounts of inputs
449 from rostrally and caudally tuned afferents, suggesting both nose-up and nose-down
450 tilts are equally detected by the VS pathway. In contrast, the vestibulo-ocular pathway
451 shows an anatomical bias for representation of nose-up body tilt (Schoppik et al., 2017).
452 This indicates that different strategies might be involved to adjust body posture and eye
453 position for pitch movements in larval zebrafish.

454 Moreover, it is important for animals to distinguish self-generated and external
455 vestibular signals. We described the direct excitatory inputs from vestibular afferents
456 onto the VS neurons during passive movements. How do self-generated motion signals
457 modulate the activities of VS neurons? Projections from Purkinje cells in the cerebellum
458 are thought to suppress sensory-evoked activity in VS neurons during voluntary self-
459 motion (Cullen, 2019). In the future, it would be interesting to use *in vivo* whole-cell
460 physiology to investigate how central vestibular neurons distinguish self-generated
461 movements from passive movements.

462 **Methods:**

463 Fish lines and husbandry:

464 *Tg(nefma:LRL:Gal4)* was established by injecting the construct containing hsp70
465 promoter (Kimura et al., 2014), and the insertion site was set at the upstream of the
466 *nefma* gene with the CRISPR target sequence: CATCGACGGATCAATGG. The
467 *Tg(nefma:gal4)* fish line was generated by crossing *Tg(nefma:LRL:Gal4)* with a
468 ubiquitous-Cre fish. The *otogc.1522+2T>A* -/- (rock solo) mutant is vestibular deficient
469 due to a splice site mutation in *otogelin* (Mo et al., 2010, Roberts et al., 2017). Rock
470 solo homozygotes on a *Tg(nefma:gal4, UAS:GFP)* background were crossed to rock
471 solo WT/heterozygotes to produce clutches containing WT, heterozygotes and
472 homozygotes for recording purposes. The rock solo homozygotes were identified by the
473 absence of anterior otolith (utricle). All experiments and procedures were approved by
474 the Animal Studies Committee at Washington University and adhere to NIH guidelines.

475 Animals were raised and maintained in the Washington University Zebrafish Facility at
476 28.5°C with a 14:10 light:dark cycle. Larval zebrafish (4-7 dpf) were housed either in
477 petri dishes or shallow tank with system water. Adult animals were maintained up to 1
478 year old with standard procedure.

479 Electrophysiology:

480 VS neurons were targeted for whole-cell patch clamp recordings based on their
481 characteristic position and fluorescence in the *Tg(nefma:gal4, UAS:GFP)* fish. The
482 larvae (4-7 dpf) were paralyzed by 0.1% α -bungarotoxin and embedded in a 10 mm
483 FluoroDish (WPI) with low-melting point agarose (Complex SeaPlaque Agarose, 2.4%
484 in system water). Fish were immersed in extracellular solution ([in mM] NaCl 134, KCl
485 2.9, MgCl₂ 1.2, HEPES 10, glucose 10, CaCl₂ 2.1, osmolarity ~295 mOsm and pH ~
486 7.5) and a small piece of skin above the brainstem was carefully removed by sharpened
487 tungsten pins. The fish was transferred to an epifluorescence microscope equipped with
488 immersion objectives (Olympus, 40x, 0.8 NA), infrared differential interference contrast
489 optics and air-bearing sled recording table.

490 Patch pipettes (7-9 M Ω) were filled with internal solution ([in mM] K gluconate 125,
491 MgCl₂ 2.5, HEPES 10, EGTA 10, Na₂ATP 4, Alexa Fluor 568 or 647 hydrazide 0.05-0.1,
492 osmolarity ~295 mOsm and pH ~ 7.5). After whole-cell configuration was achieved,
493 voltage clamp and current clamp signals were recorded at room temperature with a
494 Multiclick 700B, filtered at 10 kHz (current clamp) or 2 kHz (voltage clamp), digitized at

495 50 kHz with Digidata 1440 (Axon Instruments), and acquired by Clampex 10 (Molecular
496 Devices).

497 Before the vestibular stimulus was delivered to the fish, the immersion objective was
498 removed from the recording chamber. During the recording, series resistance was
499 monitored every 15 s to ensure good recording quality; neurons with series resistance
500 variation > 25% were discarded. After recording, the recorded cell was imaged with
501 epifluorescence to confirm cell identity.

502 Vestibular stimulation:

503 The recording rig was custom-designed to allow delivering user-controlled movement to
504 the fish during recording without losing whole-cell access. The microscope and a one-
505 axis or two-axis air-bearing sled (Aerotech, ABL1500WB or ABL1500&1500WB) were
506 fixed on an air table. Manipulators (Microstar) and recording platform (ThorLab) were
507 positioned on the sled. The sled was powered with the Aerotech transformers (TM5),
508 NPdrivers (NDRIVECP10-MXU&NDRIVECP20-MXU) and nitrogen gas (Airgas, NI
509 UHP300). Stimuli were designed in Matlab and imported into the program by Aerotech
510 software (Motion Designer/Composer), with additional tuning as required to compensate
511 for the motion of the underlying air table. Movement was recorded by an accelerometer
512 (Sparkfun, ADXL335) attached to the platform. Motion signals were digitized at 50 kHz
513 with Digidata 1440 (Axon Instruments), and acquired in Clampex 10 (Molecular
514 Devices).

515 Fish were embedded either dorsal side up (movements on rostral-caudal and ipsilateral-
516 contralateral axes) or left/right side up (movements on dorsal-ventral and rostral-caudal
517 axes) and a series of frequency-varying sinusoidal translational stimulus was applied.
518 The stimulus amplitude was set at 0.02 g or 0.06 g (min to max: 0.04 g or 0.12 g
519 respectively), and stimulus frequency range was 0.5-8 Hz. For spatial tuning
520 measurements, linear translation was applied on four different axes (0-180°, 45°-225°,
521 90°-270°, 135°-315°) on the horizontal plane. To record spike tuning in neurons without
522 spontaneous firing, a rheobase current was injected to depolarize the cell.

523 Vestibular afferent stimulation and pharmacology

524 A glass pipette electrode (2-5 MΩ) filled with extracellular solution ([in mM] NaCl 134,
525 KCl 2.9, MgCl₂ 1.2, HEPES 10, glucose 10, CaCl₂ 2.1, osmolarity ~295 mOsm and pH ~
526 7.5) was connected to a stimulator (A-M systems, Model 2100), and placed in the
527 vestibular ganglion to stimulate the vestibular afferents. A train of 0.1 ms, 1 μA - 1 mA
528 electrical pulses at varying frequencies were delivered to elicit EPSCs in the recorded
529 cells. At least 20 trials of evoked EPSCs were recorded to establish a stable baseline.
530 AMPA receptors and gap junctions were blocked with 10 μM NBQX and 500 μM
531 carbenoxolone, respectively.

532 Electron Microscopy:

533 Ultrathin serial sections of brainstem from a 5.5 dpf zebrafish were a generous loan
534 from J. Lichtman and F. Engert. Using the published 18.8 nm/px reference map and
535 reconstructions (Hildebrand et al., 2017), we targeted re-imaging at 4 nm/px to the

536 entirety of the myelinated utricular afferents (identified by their peripheral processes
537 reaching for the utricular macula) and VS neurons (identified by their position and
538 axonal projections into the spinal cord) on one side of the brainstem, covering $\sim 95 \mu\text{m}$
539 in the rostrocaudal axis. Imaging was carried out on a Zeiss Merlin 540 FE-SEM with a
540 solid-state backscatter detector. The ATLAS scan engine was controlled via
541 WaferMapper (Hayworth et al., 2014). The resulting images were aligned onto the 18.8
542 nm/px dataset using linear affine transformations in FIJI with the TrakEM2 plug-in
543 (Cardona et al., 2012) and will be freely available after publication. In a small subset of
544 identified synapses, we carried out further re-imaging at 1nm/px to visualize the
545 hallmarks of gap junctions.

546 The existing tracings of VS neurons and utricular afferents were extended to cover
547 branches that had been missed or untraced in the original dataset. Afferent/VS neuron
548 appositions were considered to be synaptic contacts if the presynapse contained
549 vesicles, the membranes were tightly apposed and straight, and there were signs of a
550 postsynaptic density. In cases where appositions were more difficult to determine, such
551 as those parallel to the plane of section, vesicle clustering at a tight apposition was used
552 as the criterion for a synapse.

553 **Analysis:**

554 All analysis are implemented in Matlab (Mathworks).

555 **Event detection:**

556 EPSC events were detected by a derivative method (Bagnall and McLean, 2014).

557 Tuning index of all EPSCs was calculated as the vectoral sum of all events' phase,
558 weighted by the EPSC amplitude.

$$559 \quad \text{Tuning index} = \frac{|\sum A_j * e^{i*\theta_j}|}{\sum A_j}, i = \sqrt{-1}$$

560 (A_j is the amplitude of each EPSC event j , and θ_j is the phase of that event relative to
561 the sinusoidal stimulus on each axis.)

562 **Deconvolution of electrical and chemical signals**

563 We assumed that the signals we observed on voltage clamp were majorly composed of
564 electrical EPSCs and chemical EPSCs from afferents, based on our observation from
565 the pharmacology data.

566

$$567 \quad S = \text{conv}(w_e, s_e) + \text{conv}(w_c, s_c) + \text{residuals}$$

568

569 (w_e , w_c are the kernels of electrical and chemical components of EPSCs, both derived
570 from their waveforms shown in Fig. 2, and s_e , s_c are the separated electrical and
571 chemical signals)

572 A sparse deconvolution algorithm with L1 regularization, derived from FISTA ((Beck and
573 Teboulle, 2009), was applied to obtain s_e, s_c by minimizing the objective function:

574
$$F(s_e, s_c) \equiv \frac{1}{2} (S_{observed} - S_{reconstruct})^2 + \lambda_e * |s_e| + \lambda_c * |s_c|,$$

575 where:

576
$$S_{reconstruct} = conv(w_e, s_e) + conv(w_c, s_c)$$

577

578 λ_e and λ_c were defined by the root mean square of the signal and magnitude of kernel

579 waveform: $\lambda_i = rms(S_{observed}) * \sqrt{w_i * w_i^T}$. Maximum iteration cycle was set at 500

580 Clustering and quantification of electrical events

581 Amplitude-invariant EPSCs are mediated by gap junctions, therefore only electrical
582 signals s_e were used to infer individual afferent inputs. A threshold of $3.5 * std(s_e)$ was
583 used for event detection. Detected electrical events were clustered by ISO-SPLIT
584 (Chung et al., 2017). Some clusters were merged or split manually after examination.
585 Clusters with refractory period (threshold: probability < 0.003 within 1 ms) in auto-
586 correlograms (100 ms) were considered from an individual afferent.

587 For each cluster, the tuning vector of inferred afferent k on each axis was quantified as:

588
$$z_k = \frac{\sum e^{i * \theta_j}}{N_c * A_s} * f_s, i = \sqrt{-1}$$

589 (θ_j is the phase of EPSC event j in cluster k . N_c is the number of cycles for sinusoidal
590 translation, f_s [Hz] and A_s [g] are the frequency and amplitude of the stimulus. The
591 absolute value and argument of z represent the tuning gain and the tuning phase,
592 respectively.)

593 Tuning in four axes was fitted into a 2-dimensional spatiotemporal model (Angelaki,
594 1992) to obtain the maximum tuning direction, the tuning gain and phase in that
595 direction.

596 Afferent inputs similarity index for a VS neuron was determined as:

597
$$\frac{|\sum A_k * z_k|}{\sum A_k * n_k}$$

598 (A_k, z_k, n_k are the average EPSC amplitude, tuning vector and number of events for
599 cluster k .)

600 AC/DC response quantification

601 AC of membrane potential and spiking response were defined as the amplitude of
602 sinusoidal fit (2 Hz) of the membrane potential, and the spike vectorial sum during
603 sensory stimulation, respectively. DC of membrane potential and spiking response were
604 defined as the average membrane potential during sensory stimulation above baseline
605 (no stimulation), and the total spike number during sensory stimulation above baseline.

606 For spiking responses, VS neurons with firing rate > 4 spike/cycle and spike AC or
607 DC >1 spike/cycle were included in the analysis.

608 Bootstrapping: $\binom{n_i}{2}$ afferent pairs were counted for VS neuron i with n_i distinct afferent
609 inputs ($n_i \geq 2$). The same number of total afferent pairs $\sum_{i=1}^m \binom{n_i}{2}$ from all m VS neurons
610 was randomly selected among all $\sum_{i=1}^m n_i$ inferred afferents to determine the
611 convergence angle or phase difference distribution by chance, and such selection was
612 performed 5000 times to calculate mean and standard deviation.

613 **Acknowledgements**

614 We thank Dr. Richard Roberts for helping set up the electrophysiology recording rig,
615 Drs. Rebecca Callahan, Mohini Sengupta and Mr. Saul Bello Rojas for thoughtful
616 critiques of the paper. We are grateful to Drs. Daniel Kerschensteiner and David
617 Schoppik for insightful comments on the manuscript. We also acknowledge the
618 Washington University Zebrafish Facility for fish care and Washington University Center
619 for Cellular Imaging (WUCCI) for supporting the confocal imaging experiments. This
620 work is supported by funding through the National Institute of Health (NIH) R00
621 DC012536 (M.W.B.), R01 DC016413 (M.W.B.), a Sloan Research Fellowship (M.W.B.),
622 and the National BioResource Project in Japan (S.H.). M.W.B. is a Pew Biomedical
623 Scholar and a McKnight Foundation Scholar.

624

625 **Author contributions:**

626 K.M and S.H generated the *Tg(gefma:gal4, UAS:GFP)* fish line. Z.L and M.B conceived
627 the project. Z.L performed the electrophysiology, confocal imaging experiments and
628 analyzed the data. T.H helped develop the deconvolution algorithm for sorting EPSC
629 events. M.B, J.M and D.H carried out the serial section EM imaging and reconstruction.
630 Z.L. and M.B wrote the manuscript with input from all other authors.

631

632 **Declaration of Interests:**

633 The authors declare no competing interests

634

635 **References:**

636 AKROUH, A. & KERSCHENSTEINER, D. 2013. Intersecting Circuits Generate Precisely Patterned
637 Retinal Waves. *Neuron*, 79, 322-334.

638 ALONSO, J. M. & MARTINEZ, L. M. 1998. Functional connectivity between simple cells and
639 complex cells in cat striate cortex. *Nature Neuroscience*, 1, 395-403.

640 ANGELAKI, D. E. 1992. SPATIOTEMPORAL CONVERGENCE (STC) IN OTOLITH NEURONS.
641 *Biological Cybernetics*, 67, 83-96.

642 ANGELAKI, D. E., BUSH, G. A. & PERACHIO, A. A. 1993. 2-DIMENSIONAL SPATIOTEMPORAL
643 CODING OF LINEAR ACCELERATION IN VESTIBULAR NUCLEI NEURONS. *Journal of*
644 *Neuroscience*, 13, 1403-1417.

645 ANGELAKI, D. E. & CULLEN, K. E. 2008. Vestibular system: The many facets of a multimodal
646 sense. *Annual Review of Neuroscience*, 31, 125-150.

647 ANGELAKI, D. E. & DICKMAN, J. D. 2000. Spatiotemporal processing of linear acceleration:
648 Primary afferent and central vestibular neuron responses. *Journal of Neurophysiology*,
649 84, 2113-2132.

650 ARENZ, A., SILVER, R. A., SCHAEFER, A. T. & MARGRIE, T. W. 2008. The contribution of single
651 synapses to sensory representation in vivo. *Science*, 321, 977-80.

652 BAGNALL, M. W., MCELVAIN, L. E., FAULSTICH, M. & DU LAC, S. 2008. Frequency-independent
653 synaptic transmission supports a linear vestibular behavior. *Neuron*, 60, 343-52.

654 BAGNALL, M. W. & MCLEAN, D. L. 2014. Modular organization of axial microcircuits in zebrafish.
655 *Science (New York, N.Y.)*, 343, 197-200.

656 BECK, A. & TEBOULLE, M. 2009. A Fast Iterative Shrinkage-Thresholding Algorithm for Linear
657 Inverse Problems. *Siam Journal on Imaging Sciences*, 2, 183-202.

658 BOYLE, R., GOLDBERG, J. M. & HIGHSTEIN, S. M. 1992. Inputs from regularly and irregularly
659 discharging vestibular nerve afferents to secondary neurons in squirrel monkey
660 vestibular nuclei. III. Correlation with vestibulospinal and vestibuloocular output
661 pathways. *J Neurophysiol*, 68, 471-84.

662 BOYLE, R. & JOHANSON, C. 2003. Morphological properties of vestibulospinal neurons in
663 primates. *Annals of the New York Academy of Sciences*, 1004, 183-195.

664 BRUNO, R. M., KHATRI, V., LAND, P. W. & SIMONS, D. J. 2003. Thalamocortical angular tuning
665 domains within individual barrels of rat somatosensory cortex. *Journal of Neuroscience*,
666 23, 9565-9574.

667 BUDELLI, R. & MACADAR, O. 1979. STATO-ACOUSTIC PROPERTIES OF UTRICULAR AFFERENTS.
668 *Journal of Neurophysiology*, 42, 1479-1493.

669 CARDONA, A., SAALFELD, S., SCHINDELIN, J., ARGANDA-CARRERAS, I., PREIBISCH, S., LONGAIR,
670 M., TOMANCAK, P., HARTENSTEIN, V. & DOUGLAS, R. J. 2012. TrakEM2 Software for
671 Neural Circuit Reconstruction. *Plos One*, 7.

672 CHABROL, F. P., ARENZ, A., WIECHERT, M. T., MARGRIE, T. W. & DIGREGORIO, D. A. 2015.
673 Synaptic diversity enables temporal coding of coincident multisensory inputs in single
674 neurons. *Nat Neurosci*, 18, 718-27.

675 CHUNG, J. E., MAGLAND, J. F., BARNETT, A. H., TOLOSA, V. M., TOOKER, A. C., LEE, K. Y., SHAH,
676 K. G., FELIX, S. H., FRANK, L. M. & GREENGARD, L. F. 2017. A Fully Automated Approach
677 to Spike Sorting. *Neuron*, 95, 1381-1394 e6.

678 CULLEN, K. E. 2019. Vestibular processing during natural self-motion: implications for
679 perception and action. *Nature Reviews Neuroscience*, 20, 346-363.

680 EATOCK, R. A. & SONGER, J. E. 2011. Vestibular hair cells and afferents: two channels for head
681 motion signals. *Annu Rev Neurosci*, 34, 501-34.

682 EHRLICH, D. E. & SCHOPPIK, D. 2017. Control of Movement Initiation Underlies the
683 Development of Balance. *Current Biology*, 27, 334-344.

684 EHRLICH, D. E. & SCHOPPIK, D. 2019. A primal role for the vestibular sense in the development
685 of coordinated locomotion. *Elife*, 8.

686 FAVRE-BULLE, I. A., VANWALLEGHEM, G., TAYLOR, M. A., RUBINSZTEIN-DUNLOP, H. & SCOTT, E.
687 K. 2018. Cellular-Resolution Imaging of Vestibular Processing across the Larval Zebrafish
688 Brain. *Curr Biol*, 28, 3711-3722 e3.

689 FAY, R. R. 1984. THE GOLDFISH EAR CODES THE AXIS OF ACOUSTIC PARTICLE MOTION IN 3
690 DIMENSIONS. *Science*, 225, 951-954.

691 FELLEMAN, D. J. & VAN ESSEN, D. C. 1991. Distributed Hierarchical Processing in the Primate
692 Cerebral Cortex. *Cerebral Cortex*, 1, 1-47.

693 FERNANDEZ, C. & GOLDBERG, J. M. 1976a. PHYSIOLOGY OF PERIPHERAL NEURONS
694 INNERVATING OTOLITH ORGANS OF SQUIRREL-MONKEY .1. RESPONSE TO STATIC TILTS
695 AND TO LONG-DURATION CENTRIFUGAL FORCE. *Journal of Neurophysiology*, 39, 970-
696 984.

697 FERNANDEZ, C. & GOLDBERG, J. M. 1976b. PHYSIOLOGY OF PERIPHERAL NEURONS
698 INNERVATING OTOLITH ORGANS OF SQUIRREL-MONKEY .3. RESPONSE DYNAMICS.
699 *Journal of Neurophysiology*, 39, 996-1008.

700 FERNANDEZ, C., GOLDBERG, J. M. & ABEND, W. K. 1972. RESPONSE TO STATIC TILTS OF
701 PERIPHERAL NEURONS INNERVATING OTOLITH ORGANS OF SQUIRREL-MONKEY. *Journal of
702 Neurophysiology*, 35, 978-+.

703 GOLDBERG, J. M., DESMADRYL, G., BAIRD, R. A. & FERNANDEZ, C. 1990. THE VESTIBULAR NERVE
704 OF THE CHINCHILLA .4. DISCHARGE PROPERTIES OF UTRICULAR AFFERENTS. *Journal of
705 Neurophysiology*, 63, 781-790.

706 HADDON, C., MOWBRAY, C., WHITFIELD, T., JONES, D., GSCHMEISSNER, S. & LEWIS, J. 1999.
707 Hair cells without supporting cells: further studies in the ear of the zebrafish mind bomb
708 mutant. *J Neurocytol*, 28, 837-50.

709 HAYWORTH, K. J., MORGAN, J. L., SCHALEK, R., BERGER, D. R., HILDEBRAND, D. G. C. &
710 LICHTMAN, J. W. 2014. Imaging ATUM ultrathin section libraries with WaferMapper: a
711 multi-scale approach to EM reconstruction of neural circuits. *Frontiers in Neural Circuits*,
712 8.

713 HILDEBRAND, D. G. C., CICCONET, M., TORRES, R. M., CHOI, W., QUAN, T. M., MOON, J.,
714 WETZEL, A. W., SCOTT CHAMPION, A., GRAHAM, B. J., RANDLETT, O., PLUMMER, G. S.,
715 PORTUGUES, R., BIANCO, I. H., SAALFELD, S., BADEN, A. D., LILLANEY, K., BURNS, R.,
716 VOGELSTEIN, J. T., SCHIER, A. F., LEE, W. A., JEONG, W. K., LICHTMAN, J. W. & ENGERT,
717 F. 2017. Whole-brain serial-section electron microscopy in larval zebrafish. *Nature*, 545,
718 345-349.

719 HUBEL, D. H. & WIESEL, T. N. 1962. RECEPTIVE FIELDS, BINOCULAR INTERACTION AND
720 FUNCTIONAL ARCHITECTURE IN CATS VISUAL CORTEX. *Journal of Physiology-London*,
721 160, 106-&.

722 JIA, H., ROCHEFORT, N. L., CHEN, X. & KONNERTH, A. 2010. Dendritic organization of sensory
723 input to cortical neurons *in vivo*. *Nature*, 464, 1307-1312.

724 KIMMEL, C. B., POWELL, S. L. & METCALFE, W. K. 1982. Brain neurons which project to the
725 spinal cord in young larvae of the zebrafish. *The Journal of comparative neurology*, 205,
726 112-27.

727 KIMURA, Y., HISANO, Y., KAWAHARA, A. & HIGASHIJIMA, S. 2014. Efficient generation of knock-
728 in transgenic zebrafish carrying reporter/driver genes by CRISPR/Cas9-mediated genome
729 engineering. *Scientific Reports*, 4.

730 KODAMA, T., GITTIS, A., SHIN, M., KELLEHER, K., KOLKMAN, K., MCELVAIN, L., LAM, M. & DU
731 LAC, S. 2020. Graded co-expression of ion channel, neurofilament, and synaptic genes in
732 fast-spiking vestibular nucleus neurons. *J Neurosci*.

733 KORN, H., SOTELO, C. & BENNETT, M. V. L. 1977. The lateral vestibular nucleus of the toadfish
734 Opsanus tau: Ultrastructural and electrophysiological observations with special
735 reference to electrotonic transmission. *Neuroscience*.

736 LAURENS, J., LIU, S., YU, X. J., CHAN, R., DICKMAN, D., DEANGELIS, G. C. & ANGELAKI, D. E. 2017.
737 Transformation of spatiotemporal dynamics in the macaque vestibular system from
738 otolith afferents to cortex. *Elife*, 6.

739 LAVZIN, M., RAPOPORT, S., POLSKY, A., GARION, L. & SCHILLER, J. 2012. Nonlinear dendritic
740 processing determines angular tuning of barrel cortex neurons in vivo. *Nature*, 490, 397-
741 401.

742 LECUN, Y., BENGIO, Y. & HINTON, G. 2015. Deep learning. *Nature*, 521, 436-444.

743 LU, Z., XU, Z. & BUCHSER, W. J. 2004. Coding of acoustic particle motion by utricular fibers in
744 the sleeper goby, *Dormitator latifrons*. *Journal of Comparative Physiology a-*
745 *Neuroethology Sensory Neural and Behavioral Physiology*, 190, 923-938.

746 MARUSKA, K. P. & MENSINGER, A. F. 2015. Directional sound sensitivity in utricular afferents in
747 the toadfish *Opsanus tau*. *Journal of Experimental Biology*, 218, 1759-1766.

748 MCELVAINE, L. E., FAULSTICH, M., JEANNE, J. M., MOORE, J. D. & DU LAC, S. 2015.
749 Implementation of linear sensory signaling via multiple coordinated mechanisms at
750 central vestibular nerve synapses. *Neuron*, 85, 1132-44.

751 MCLEAN, D. L. & FETCHO, J. R. 2009. Spinal Interneurons Differentiate Sequentially from Those
752 Driving the Fastest Swimming Movements in Larval Zebrafish to Those Driving the
753 Slowest Ones. *Journal of Neuroscience*, 29, 13566-13577.

754 MIGAULT, G., VAN DER PLAS, T. L., TRENTESAUX, H., PANIER, T., CANDELIER, R., PROVILLE, R.,
755 ENGLITZ, B., DEBREGEAS, G. & BORMUTH, V. 2018. Whole-Brain Calcium Imaging during
756 Physiological Vestibular Stimulation in Larval Zebrafish. *Curr Biol*, 28, 3723-3735 e6.

757 MO, W., CHEN, F. Y., NECHIPORUK, A. & NICOLSON, T. 2010. Quantification of vestibular-
758 induced eye movements in zebrafish larvae. *Bmc Neuroscience*, 11.

759 NAGY, J. I., BAUTISTA, W., BLAKLEY, B. & RASH, J. E. 2013. Morphologically mixed chemical-
760 electrical synapses formed by primary afferents in rodent vestibular nuclei as revealed
761 by immunofluorescence detection of connexin36 and vesicular glutamate transporter-1.
762 *Neuroscience*, 252, 468-88.

763 NEUHUBER, W. L. & ZENKER, W. 1989. CENTRAL DISTRIBUTION OF CERVICAL PRIMARY
764 AFFERENTS IN THE RAT, WITH EMPHASIS ON PROPRIOCEPTIVE PROJECTIONS TO
765 VESTIBULAR, PERIHYPOGLOSSAL, AND UPPER THORACIC SPINAL NUCLEI. *Journal of*
766 *Comparative Neurology*, 280, 231-253.

767 NEWLANDS, S. D. & PERACHIO, A. A. 2003. Central projections of the vestibular nerve: a review
768 and single fiber study in the Mongolian gerbil. *Brain Research Bulletin*, 60, 475-495.

769 ORLOVSKY, G. N. 1972. ACTIVITY OF VESTIBULOSPINAL NEURONS DURING LOCOMOTION. *Brain*
770 *Research*, 46, 85-&.

771 PETERSEN, C. C. H. 2007. The functional organization of the barrel cortex. *Neuron*, 56, 339-355.

772 PETERSON, B. W. 1970. Distribution of neural responses to tilting within vestibular nuclei of the
773 cat. *J Neurophysiol*, 33, 750-67.

774 PLATT, C. 1977. HAIR CELL DISTRIBUTION AND ORIENTATION IN GOLDFISH OTOLITH ORGANS.
775 *Journal of Comparative Neurology*, 172, 283-297.

776 PRIEBE, N. J. & FERSTER, D. 2012. Mechanisms of Neuronal Computation in Mammalian Visual
777 Cortex. *Neuron*, 75, 194-208.

778 PRIEBE, N. J., MECHLER, F., CARANDINI, M. & FERSTER, D. 2004. The contribution of spike
779 threshold to the dichotomy of cortical simple and complex cells. *Nature Neuroscience*, 7,
780 1113-1122.

781 RILEY, B. B. & MOORMAN, S. J. 2000. Development of utricular otoliths, but not saccular
782 otoliths, is necessary for vestibular function and survival in zebrafish. *J Neurobiol*, 43,
783 329-37.

784 ROBERTS, R., ELSNER, J. & BAGNALL, M. W. 2017. Delayed Otolith Development Does Not
785 Impair Vestibular Circuit Formation in Zebrafish. *J Assoc Res Otolaryngol*, 18, 415-425.

786 ROY, N. C., BESSAIH, T. & CONTRERAS, D. 2011. Comprehensive mapping of whisker-evoked
787 responses reveals broad, sharply tuned thalamocortical input to layer 4 of barrel cortex.
788 *Journal of Neurophysiology*, 105, 2421-2437.

789 SARKISIAN, V. H. 2000. Input-output relations of Deiters' lateral vestibulospinal neurons with
790 different structures of the brain. *Archives Italiennes De Biologie*, 138, 295-353.

791 SCHOPPIK, D., BIANCO, I. H., PROBER, D. A., DOUGLASS, A. D., ROBSON, D. N., LI, J. M. B.,
792 GREENWOOD, J. S. F., SOUCY, E., ENGERT, F. & SCHIER, A. F. 2017. Gaze-Stabilizing
793 Central Vestibular Neurons Project Asymmetrically to Extraocular Motoneuron Pools. *J
794 Neurosci*, 37, 11353-11365.

795 SCHOR, R. H., MILLER, A. D. & TOMKO, D. L. 1984. Responses to head tilt in cat central
796 vestibular neurons. I. Direction of maximum sensitivity. *J Neurophysiol*, 51, 136-46.

797 SHERMAN, S. M. 2005. Thalamic relays and cortical functioning. In: CASAGRANDE, V. A.,
798 GUILLYERY, R. W. & SHERMAN, S. M. (eds.) *Cortical Function: a View from the Thalamus*.

799 SKOTTUN, B. C., DE VALOIS, R. L., GROSOF, D. H., MOVSHON, J. A., ALBRECHT, D. G. & BONDS,
800 A. B. 1991. Classifying simple and complex cells on the basis of response modulation.
801 *Vision Res*, 31, 1079-86.

802 SMEAR, M. C., TAO, H. Z. W., STAUB, W., ORGER, M. B., GOSSE, N. J., LIU, Y., TAKAHASHI, K.,
803 POO, M. M. & BAIER, H. 2007. Vesicular glutamate transport at a central synapse limits
804 the acuity of visual perception in zebrafish. *Neuron*, 53, 65-77.

805 STRAKA, H. & DIERINGER, N. 1996. Uncrossed disynaptic inhibition of second-order vestibular
806 neurons and its interaction with monosynaptic excitation from vestibular nerve afferent
807 fibers in the frog. *Journal of Neurophysiology*, 76, 3087-3101.

808 TOMKO, D. L., PETERKA, R. J. & SCHOR, R. H. 1981. RESPONSES TO HEAD TILT IN CAT 8TH NERVE
809 AFFERENTS. *Experimental Brain Research*, 41, 216-221.

810 TURECEK, J., JACKMAN, S. L. & REGEHR, W. G. 2017. Synaptotagmin 7 confers frequency
811 invariance onto specialized depressing synapses. *Nature*, 551, 503-506.

812 USREY, W. M., REPPAS, J. B. & REID, R. C. 1999. Specificity and strength of retinogeniculate
813 connections. *Journal of Neurophysiology*, 82, 3527-3540.

814 VOESENEK, C. J., PIETERS, R. P. M. & VAN LEEUWEN, J. L. 2016. Automated Reconstruction of
815 Three-Dimensional Fish Motion, Forces, and Torques. *Plos One*, 11.

816 WILENT, W. B. & CONTRERAS, D. 2005. Dynamics of excitation and inhibition underlying
817 stimulus selectivity in rat somatosensory cortex. *Nature Neuroscience*, 8, 1364-1370.

818 WITTS, E. C. & MURRAY, A. J. 2019. Vestibulospinal contributions to mammalian locomotion.
819 *Current Opinion in Physiology*, 8.

820